Cloud tomography applied to sky images: A virtual testbed

Felipe A Mejia, Ben Kurtz, Aviad Levis, Íñigo de la Parra, Jan Kleissl

Keywords: 3D Cloud Reconstruction, Tomography, Cloud Optical Depth, Sky Imager, Solar Forecasting

Center for Renewable Resources and Integration, Department of Mechanical and Aerospace Engineering, University of California, San Diego 9500 Gilman Dr., La Jolla, CA 92093, USA

Abstract

Two tomographic techniques are applied to two simulated sky images with different cloud fraction. The Algebraic Reconstruction Technique (ART) is applied to optical depth maps from sky images to reconstruct 3-D cloud extinction coefficients without considering multiple scattering effects. Reconstruction accuracy is explored for different products, including surface irradiance and extinction coefficients, as a function of the number of available sky imagers and setup distance. Increasing the number of imagers improves the accuracy of the 3-D reconstruction: for surface irradiance, the error decreases significantly up to four imagers at which point the improvements become marginal. But using nine imagers gives more robust results in practical situations in which the circumsolar region of images has to be excluded due to poor cloud detection. The ideal distance between imagers was also explored: for a cloud height of 1 km, increasing distance up to 3 km (the domain length) improved the 3-D reconstruction. An iterative reconstruction technique that iteratively updated the source function improved the results of the ART by minimizing the error between input red radiance images and reconstructed red radiance simulations. For the best case of a nine-imager deployment, the ART and iterative method resulted in 53.4% and 33.6% mean absolute error for the extinction coefficients, respectively.

Nomenclature

Abbreviations		**Variables**	
AERONET	Aerosol Robotic Network	$\mathcal{A}$	Matrix relating $\boldsymbol{k}$ to $\boldsymbol{\tau_p}$ [-]
AirMISR	Airborne multi-angle imaging spectroradiometer	$\boldsymbol{a}_p$	p-th row of matrix $\mathcal{A}$ [-]
ART	Algebraic reconstruction technique	f	Focal length [m]
CBH	Cloud base height	I	Radiance [$\mathrm{W \cdot sr^{-1} \cdot m^{-2}}$]
CF	Cloud fraction.	I^{meas}	Ground truth radiance from LES input into SHDOM [$\mathrm{W \cdot sr^{-1} \cdot m^{-2}}$]
CTH	Cloud top height	I_0	Emitted radiance [$\mathrm{W \cdot sr^{-1} \cdot m^{-2}}$]
DNI	Direct normal irradiance	i	Gradient descent iterative step [-]
GHI	Global horizontal irradiance	J	Source Function [$\mathrm{W\ m^{-2}\ sr^{-1}\ Hz^{-1}}$]
MAE	Mean absolute error	j	Iterative index [-]
MBE	Mean bias error	k	Extinction coefficient [$\mathrm{m^{-1}}$]
MWR	Microwave radiometer	$\boldsymbol{k}$	Matrix of all extinction coefficients in domain [-]
LES	Large eddy simulation	$\boldsymbol{k^s}$	Vector of extinction coefficients along a view path [-]

PB	Pixel brightness	$\boldsymbol{k}_{LES}$	Matrix of extinction coefficients from LES [-]
RRBR	Radiance Red-Blue Ratio	L	Distance between sky imagers [m]
SHDOM	Spherical harmonic discrete ordinate method	LWC	Liquid water content [kg m^{-3}]
SI	Sky imagers	m	Index in the vertical (z) direction [-]. $m = 1, \dots, N_z$
SZA	Solar zenith angle	p	Pixel index [-]. p = 1, …, P, where P is the number of sky image pixels.
		$\boldsymbol{N_z}$	Number of elements vertical levels in the domain [-]
		r'	Distance from the principal point in the image plane [m]
		$\boldsymbol{s}$	Position vector along the view path [m]
		w	Weighting factor [-]
		γ	Iterative step size [-]
		ϑ	Zenith angle [°]
		$\boldsymbol{\vartheta}_p$	Vector of all zenith angle of all pixels [°]
		ϑ_s	Scattering angle [°]
		τ	Optical path [m]
		$\boldsymbol{\tau}_p$	Vector of optical path of all pixels [m]
		ϕ	Azimuth [°]
		$\boldsymbol{\phi}_p$	Vector of all azimuth of all pixels [°]
		$\boldsymbol{\theta}$	Phase function [°]
		ω	Single scattering albedo [-]
		$\boldsymbol{\omega}_d$	Unit vector of direction [-]

1. Introduction

The transition from conventional fossil energy to renewable energy has been aided by continued improvements in renewable technologies, but this progress is met with new challenges. Unlike conventional energy sources, which provide steady and reliable power output, solar energy generation requires larger regulation by ancillary generators to balance generation and demand during periods of high variability. Accurate forecasting of these periods of high variability will support management of the electric grid and electricity markets and, therefore, ensure a more economical integration of solar power (Mathiesen et al., 2013). Currently, several different methods are used to forecast at different spatial and temporal resolutions, including numerical weather prediction (Lorenz et al., 2009; Mathiesen and Kleissl, 2011) and satellite image-based forecasting (Hammer et al., 1999). Whole-sky imagery is the method of choice for short term forecasting (up to 15 minutes, e.g. Urquhart et al., (2013)). Physics-based solar forecasting using sky imagery (SI) has three main components: identifying clouds, advecting them, and calculating the solar energy that reaches the ground under the advected cloud field. Most algorithms assume that clouds exist as plane cloud at the cloud base height (CBH). In other words, the cloud geometric thickness is assumed to be negligible, which leads to projection errors (Kurtz et al., 2017). A perfect representation of the cloud field requires a 3-D matrix of cloud extinction coefficients $\boldsymbol{k}(x,y,z)$ in the atmosphere.

Basic geometric cloud information has been derived in a few papers. CBH was obtained from stereography applied to two sky imagers by Nguyen and Kleissl (2014). Although CBH is a crucial aspect of the 3-D geometric description of a cloud, it does not completely describe the cloud properties. Peng et al. (2015) expanded on this concept by providing a variable CBH for different cloud layers using multiple cameras but still assumed a negligible cloud geometric thickness. The cloud voxel technique in Oberländer et al. (2015) provides 3-D cloud shape but does not provide extinction coefficients within the cloud; therefore it is not possible to calculate the resulting radiance field from first physical principles.

Stereographic techniques have already been used to obtain 3-D atmospheric water vapor distribution from ground-based GPS observations (Huang et al., 2008; Wu et al., 2017; Ye et al., 2016). Huang et al. (2008) revisited the cloud tomography technique and examined the mathematical nature of the retrieval problem and its relationship to the physical configuration of microwave radiometers. Levis et al. (2015) applied an iterative tomographic technique to Airborne Multiangle SpectroPolarimetric Imager (AirMSPI) aircraft measurement to retrieve cloud extinction coefficients. The iterative method minimizes the difference between radiance in a simulated image and a ground-truth image. The cloud domain is discretized, and a system of linear equations is set up to relate $\boldsymbol{k}$ to radiation measured by microwave radiometers (MWRs). Levis et al. (2015) obtain a 33% mean absolute error (MAE) with a 22.2 m and 44.4 m horizontal and vertical resolution, respectively.

In this paper, we will implement the iterative tomographic technique of Levis et al. (2015) to identify 3-D cloud extinction coefficients from sky images. Since iterative tomography is computationally too expensive for real-time solar forecasting, a faster technique called algebraic reconstruction is applied first and then used to initialize the iterative method. The tomographic methods and the synthetic cloud field is presented in Section 2. Section 3 describes the application of the tomographic methods. Section 4 presents results for the reconstruction of two synthetic sky images of different cloud fraction, and Section 5 presents discussion and conclusions. Aides et al., (2013) and Holodovsky et al., (2016) applied a sky-imagery tomographic approach for meteorological applications. This is the first time sky-imagery tomographic techniques are considered for solar forecasting, allowing forecasts to fully describe 3-D cloud effects and overcoming the constraints of the flat-plane assumption.

2. 3-D Reconstruction Methodology

2.1 Basic Principle

Our setup is passive, using the steady, uniform and collimated sun as the radiation source. To uniquely define a 3-D cloud scene, we need to know the extinction coefficients ($\boldsymbol{k}$) throughout the cloud scene. Similar problems exist in medical imaging, archaeology and generally in remote sensing and are known as computed tomography (Seeram, 2015). To solve for $\boldsymbol{k}$, tomographic techniques relate measurements of transmission to $\boldsymbol{k}$ as,

$$I = I_0 e^{-\int \boldsymbol{k}(s)ds} = I_0 e^{-\tau}, \quad (1)$$

where I is the transmitted or attenuated radiance, I_0 is the emitted radiance (from the sun), $\boldsymbol{s}$ is the path along the beam, and τ is the line integral of $\boldsymbol{k}$ or optical path. With multiple transmission measurements at different orientations, the extinction coefficients can be determined. For cloud tomography, we solve for $\boldsymbol{k}$ of the 3-D cloud field from measurements of I by multiple sky imagers.

2.2. Algebraic Reconstruction Technique

In the atmospheric sciences, clouds were reconstructed by tomographic techniques from n MWR measurements of $\boldsymbol{\tau} = (\tau_1, \tau_2, \dots, \tau_n)$ from various directions. Discretizing the domain yields the following matrix equation (Huang et al., 2008):

$$\boldsymbol{\mathcal{A}k} = \boldsymbol{\tau}\,, \tag{2}$$

where the vector of extinctions coefficients $\boldsymbol{k} = (k_1, k_2, \dots, k_n)$ is obtained by solving the system of linear equations. For notational conciseness and since most computations for each sky imager pixel and each sky imager are computationally independent, we generally denote physical 2-D variables such as sky imager optical path measurements using 1-D vectors of dimension P, and physical 3-D variables such as the extinction coefficient field as 2-D matrices of dimension $P \times N_{\mathrm{z}}$, where P is the number of pixels in the 2-D image and N_{z} is the number of vertical levels. Most equations are applied for each sky imager sequentially, but for notational conciseness we drop the 'si' index for all variables (except for Eqs. 3 and 4). For the application with sky imagers, $\boldsymbol{\tau}$ is the vector of optical paths derived from the Radiance Red Blue Ratio (RRBR) method (Mejia et al., 2016) and p is the sky imager pixel index ($p = 1, \dots, P$). The RRBR method uses a look-up table created from homogenous (overcast) cloud images to estimate $\boldsymbol{\tau}_{\mathrm{p}}$ for each pixel. Thus, $\boldsymbol{\tau}$ is a vector of individual scalar $\boldsymbol{\tau}_{\mathrm{p}}$ along the path defined by a pixel in a sky image at the pixel zenith angle ($\boldsymbol{\vartheta}_p$, or view angle) and azimuth **(**$\boldsymbol{\phi}_p$).

We approximate line integrals by assuming that only one grid cell contributes at each z level, such that $\boldsymbol{\mathcal{A}}$ is a matrix with ones when the element $\mathcal{A}_{p,m}$ satisfies the following equalities:

$$x_{p,m} = \mathrm{nearest}(z_m \tan(\boldsymbol{\vartheta}_p) \sin(\boldsymbol{\phi}_p) + x_{\mathrm{si}}) \tag{3}$$

$$y_{p,m} = \mathrm{nearest}(z_m \tan(\boldsymbol{\vartheta}_p) \cos(\boldsymbol{\phi}_p) + y_{\mathrm{si}}), \tag{4}$$

and $\mathcal{A}_{p,m} = 0$ elsewhere. $m = 1, \dots, N_z$ is the index in the vertical (z) direction, and x_{si} and y_{si} are the horizontal coordinates of the SI location. We assume $z_{\mathrm{si}} = 0$. 'nearest()' represents rounding to the nearest grid point. In this way, a sparse matrix that reduces the computational cost of solving the system of equations is obtained. An example of matrix $\boldsymbol{\mathcal{A}}$ obtained from applying Eqs. (3) and (4) is demonstrated in Figure 1 for one SI pixel.

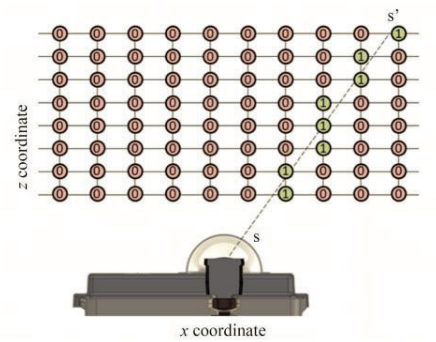

Figure 1. Conceptual diagram of ray tracing to create matrix $\boldsymbol{\mathcal{A}}$ in Eq. 2 for one SI pixel along the view path $\boldsymbol{s}$. $\boldsymbol{\mathcal{A}}$ is a 3-D matrix, but here only a vertical slice in x-z is shown. Numbers in the circles denote the values of $\boldsymbol{\mathcal{A}}$.

To solve this system of equations in Eq. 2, we will use the algebraic reconstruction technique (ART) of Gordon et al., (1970). ART is a family of algorithms to reconstruct $\boldsymbol{k}$ by solving a system of linear equations. The conventional ART method iteratively adjusts $\boldsymbol{k^s}$ (the extinction coefficient vector along a view path $\boldsymbol{s}$ associated with pixel p) as,

$$\boldsymbol{k}_{\mathrm{j}}^{\boldsymbol{s}} = \boldsymbol{k}_{\mathrm{j-1}}^{\boldsymbol{s}} + \frac{\tau_{\mathrm{p}} - \boldsymbol{a}_{\mathrm{p}} \cdot \boldsymbol{k}}{\|\boldsymbol{a}_{\mathrm{p}}\|^2} \boldsymbol{a}_{\mathrm{p}}, \quad (5)$$

where $\boldsymbol{a}_{\mathrm{p}}$ is the p-th row of the matrix $\boldsymbol{\mathcal{A}}$, $\boldsymbol{a}_{\mathrm{p}}$ maps one pixel in an image to the $\boldsymbol{k^s}$ along its view path, and j is the iterative index. Our implementation slightly differs by iteratively adjusting $\boldsymbol{k}$ as,

$$\boldsymbol{k}_{\mathrm{j}}^{\boldsymbol{s}} = \boldsymbol{k}_{\mathrm{j-1}}^{\boldsymbol{s}} \left[1 + w\left(\frac{\tau_{\mathrm{p}}}{\boldsymbol{a}_{\mathrm{p}} \cdot \boldsymbol{k}} - 1\right)\right], \quad (6)$$

where w is a weighting factor that is empirically set to 0.2. Eq. 6 is preferred over Eq. 5 as it naturally limits $\boldsymbol{k}$ to only positive values as opposed to the original ART method. Eq. 6 is first applied to all pixels of one sky imager ($p = 1, \ldots, P$), then sequentially to the other sky imagers, and then j increments by one and the process repeats until convergence. The 3-D $\boldsymbol{k}$ matrix is continually updated with the solutions $\boldsymbol{k}_{\mathrm{j}}^{\boldsymbol{s}}$. The solution $\boldsymbol{k}_{\mathrm{j}}^{\boldsymbol{s}}$ is further constrained by requiring $\boldsymbol{k}_{\mathrm{j}}^{\boldsymbol{s}} = 0$ when $\boldsymbol{\tau}_p = 0$ consistent with Oberlander et al. (2015), which ensures more accurate solutions with less computational effort. When a pixel in a different sky imager is considered, the elements of $\boldsymbol{k}$ that were already marked as clear by another sky imager will not be included in the ART update of $\boldsymbol{k}$ (Figure 2). This constraint is analogous to geometrical space-carving (Veikherman et al., 2015).

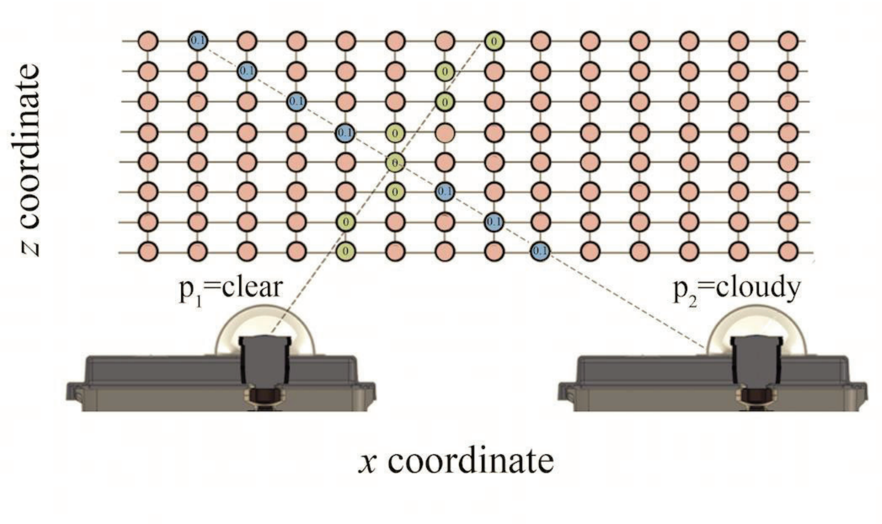

Figure 2: Conceptual diagram of ray tracing to create matrix $\boldsymbol{k}$ in Eq. 2 for two SI pixel along two view paths. The left sky imager pixel p_1 shows clear skies and all extinction coefficients along the associated view path are set to zero. The right sky imager shows a cloud in pixel p_2 and (initially) constant extinction coefficients are introduced along the associated view path, except along known clear grid points. $\boldsymbol{k}^s$ elements of 0.1 are chosen randomly here.

2.3. Iterative Retrieval

The ART method does not directly account for the effects of 3-D scattering. Therefore, non-local effects leading to adjustment of the extinction coefficients are unaccounted for. To improve the ART results, the iterative approach developed by Levis et al. (2015) for satellite data is implemented to sky images. After initializing $\boldsymbol{k}$ with the ART, the domain is simulated in a radiative transfer model. A gradient descent is applied iteratively to $\boldsymbol{k}$ to minimize the difference between measured transmitted radiance I^{meas} and the transmitted radiance simulated by Spherical Harmonic Discrete Ordinate Method (SHDOM), I (Aides et al., 2013; Levis et al., 2017; Veikherman et al., 2015).

As background consider the integral form of the radiative transfer equation,

$$I(\boldsymbol{s},\boldsymbol{\omega}_d) = \exp\left[-\int_0^s \boldsymbol{k}(\boldsymbol{s}')d\boldsymbol{s}'\right] I\left((x_{\mathrm{SI}}, y_{\mathrm{SI}}), \boldsymbol{\omega}_d\right) + \int_0^s \exp\left[-\int_s^{s'} \boldsymbol{k}(t)dt\right] J(\boldsymbol{s}',\boldsymbol{\omega}_d)\boldsymbol{k}(\boldsymbol{s}')d\boldsymbol{s}', \quad (7)$$

where $I\left((x_{SI}, y_{SI}), \boldsymbol{\omega}_d\right)$ is extraterrestrial radiance at a ground location $(x_{\mathrm{SI}}, y_{\mathrm{SI}})$ incident from direction $\boldsymbol{\omega}_d$, $\int_{\boldsymbol{s}}^{s'} \boldsymbol{k}(t)dt$ is a line integral over a field k along the segment extending from s to s' illustrated as the dashed line in Figure 1, $\boldsymbol{\omega}_d$ is the unit vector representing the direction of the view path, t is a dummy variable for integration, and J is the source function, which contributes the non-local scattering effects. Neglecting emission from the cloud, the source function J is

$$J(\boldsymbol{s},\boldsymbol{\omega}_d) = \frac{\omega}{4\pi}\int_0^{4\pi} I(\boldsymbol{s},\boldsymbol{\omega}'_d)\boldsymbol{\theta}(\boldsymbol{s};\boldsymbol{\omega}_d,\boldsymbol{\omega}'_d)d\boldsymbol{\omega}'_d, \quad (8)$$

where ω is the single scattering albedo and $\boldsymbol{\theta}(\boldsymbol{s};\boldsymbol{\omega}_d,\boldsymbol{\omega}'_d)$ is the phase function at $\boldsymbol{s}$. The phase function describes the fraction of energy scattered from $\boldsymbol{\omega}'_d$ to $\boldsymbol{\omega}_d$ by an infinitesimal volume (Levis et al., 2015). Eq. 7 shows that I explicitly depends on $\boldsymbol{k}$ along the view path. When discretized, I then only depends on the $\boldsymbol{k}$ located along that I view path as illustrated in Figure 1. This integral of $\boldsymbol{k}$ in Eq. 7 is easily iterated to minimize $I^{\mathrm{meas}} - I$ (described in Eq. 9 below), but J causes the iterative process for one direction to depend on the iterations at all other angles through 3-D scattering effects. I also implicitly depends on $\boldsymbol{k}$ through J, because scattering anywhere in the domain can increase J at a particular view path. J depends on the I in all directions such that iterating neighboring pixels affect all other pixels due to multiple scattering of radiation within and between clouds.

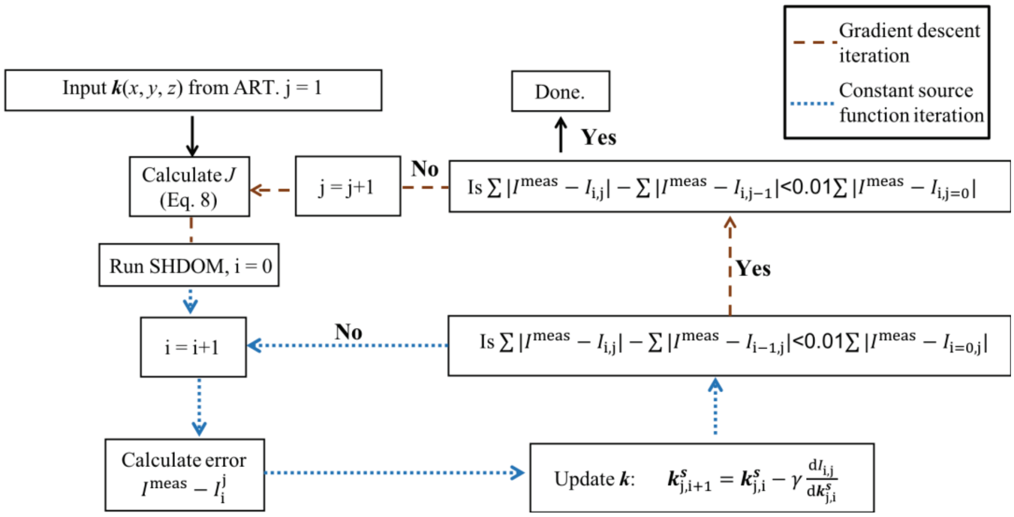

Figure 3. Flow chart of the iterative retrieval method. Dotted and dashed arrows correspond to gradient descent and constant source function iterations, respectively.

Figure 3 demonstrates the flow chart of the implementation of this iterative method. Since a more accurate initialization decreases the computational cost, $\boldsymbol{k}$ from the ART method is input to the iterative method. In the inner loop optimization (dotted arrows) a constant J is assumed. Then $I^{\text{meas}} - I$ is minimized iteratively by adjusting $\boldsymbol{k}$ at the grid points along $\boldsymbol{s}$ following a gradient descent method as

$$\boldsymbol{k}_{\text{j,i}+1}^{s} = \boldsymbol{k}_{\text{j,i}}^{s} - \gamma\frac{\text{d}I_{\text{i,j}}}{\text{d}\boldsymbol{k}_{\text{j,i}}^{s}}, \tag{9}$$

where j is the constant source function iterative step, i is the gradient descent iterative step, and γ is the step size. Eq. 9 is repeated for all pixels in a sky image (p = 1, …, P), and then for all sky imagers, and this is repeated until convergence. Convergence is met when the change in the total image error is less than 1% of the original error following

$$\sum\left|I^{\text{meas}} - I_{\text{i,j}}\right| - \sum\left|I^{\text{meas}} - I_{\text{i}-1,\text{j}}\right| < 0.01\sum\left|I^{\text{meas}} - I_{\text{i}=0,\text{j}}\right|, \tag{10}$$

where $\sum$ represents summation over all pixels in all images. Once Eq. 10 is satisfied, we recalculate J until the change in the total image error decreases to 1% of the original error:

$$\sum|I^{\text{meas}} - I_{\text{i,j}}| - \sum|I^{\text{meas}} - I_{\text{i,j}-1}| < 0.01\sum|I^{\text{meas}} - I_{\text{i,j}=0}|. \tag{11}$$

2.4. Constraining Cloud Base and Cloud Top Height

Two critical pieces of information obtained from cloud reconstruction are the CBH and cloud top height (CTH) (Sun et al., 2016; Wang et al., 2016). Figure 4a shows one of the cloud scenes with a CTH of 1.2 km, a CBH of 820 m and Figure 4b and c show the ART results. Cloud artifacts are erroneously reconstructed below and above the real cloud layer, for example at x = 1.5 km and x = 4.3 km in the unconstrained ART method in Figure 4b. In general, artifacts occur because Eq. 6 is ill-conditioned due to a lack of different perspectives for some $\boldsymbol{k}$ points. A lack of different perspectives can result from large CBH relative to the imager spacing L, i.e. large CBH / L. If none of the imagers 'sees' the air immediately above the cloud, the reconstruction lacks sufficient information to clear these areas of clouds resulting in vertical lines or cones in the reconstructed image. To remove these artifacts, we assume that no clouds are present 250 m below the CBH or 250 m above the CTH (Figure 4c). The CBH and CTH are the heights of the highest and lowest non-zero extinction coefficients calculated from the Large Eddy Simulation (LES) results. The height restriction could also be applied in practice, although it would be limited to situations with single cloud layers. For example, ceilometers can determine the CBH with an accuracy better than 250 m. Estimating CTH in practice is more challenging, however CTH (and CBH) could be estimated with temperature and humidity profiles from radiosondes (Zhong et al., 2017).

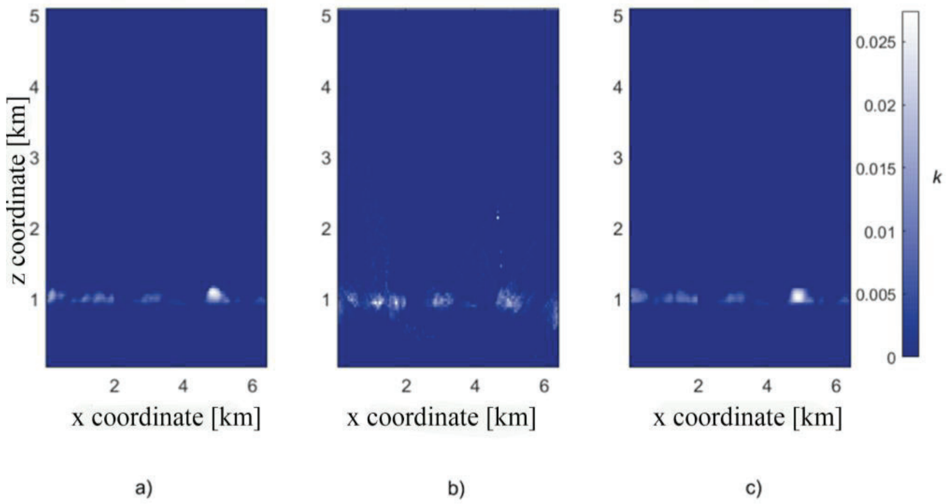

Figure 4. 2-D slice through ***k*** averaged along the *y*-axis from a) Large Eddy Simulation (LES); b) Reconstruction with 9 sky imagers separated by 1.5 km using the Algebraic Reconstruction Technique (ART) method; and c) improved reconstruction with cloud base and top height constraints.

3. Testing Layout

3.1. Objective and Domain Size

The objective is to reconstruct the 3D extinction coefficient ***k****(x,y,z)* within a solar forecast domain from sky images. The improved accuracy of the initial state is expected to result in more accurate short-term forecasts. Sky imagers can provide valuable solar forecast information up to 15 min ahead depending on cloud speed, cloud height, and cloud dynamics (Chow et al., 2015; Martín and Trapero, 2015; Quesada-Ruiz et al., 2014; Schmidt et al., 2015; Sun et al., 2016). Given that cloud speeds from the LES described in Section 3.2 vary between 8 to 10 m/s, domains should be on the order of 5 to 10 km. We chose a cloud domain of 6.4 by 6.4 km horizontal and 5 km vertical size with 50 m horizontal and 40 m vertical resolution for a total of 2,080,768 ***k*** points.

Perfect 3D reconstruction requires that all sky imager cameras are geometrically and photometrically calibrated. Geometric calibration ensures accurate georeferencing of view paths for a single imager and for a cloud or clear space observed by two imagers and techniques for accurate in-situ geometric calibration exist (Urquhart et al., 2016). Photometric calibrations ensure that red-green-blue pixel brightnesses are uniquely and accurately converted to optical depths. We acknowledge that in practice sky imagers are rarely photometrically calibrated in an absolute sense (the only known evaluation of photometric properties is presented in Urquhart et al., (2015). But as long as sky imagers are photometrically calibrated *relative* to each other, the reconstruction could be used to derive relative extinction coefficients from sky imagers and geometrically constrain clouds. Since all radiances at the ground depend linearly on the incident radiation at the top of the reconstruction domain, measurements from a single calibrated pyranometer in the domain could then be used for absolute calibration of the extinction coefficients.

Another objective is to investigate the sensitivity of the tomographic techniques to different deployment configuration variables, specifically the number of imagers and the distance between imagers. It is expected that the reconstruction accuracy improves with more imagers, but at the expense of acquisition, setup, and maintenance of additional equipment. Therefore, if additional improvements are marginal, less sky imagers would be preferred. The sensitivity to cloud fraction is also examined. Unless they are near zenith of a sky image, even clouds in a single cloud layer can block the views of other clouds behind them and deteriorate reconstruction accuracy. In the extreme case of overcast conditions, 3D reconstruction would become impossible as no image information of the cloud top is available.

The sensitivity study would be compromised by τ_p errors in the RRBR method which are used to assign cloud optical depth to each sky imager pixel and associated view path. For example, it is well documented that clouds are more difficult to detect in the circumsolar region (Yang et al., 2014) and that deployments with fewer clouds in the circumsolar region will perform better. We prevent random errors associated with the location of the clouds relative to the cameras by using a perfect $\boldsymbol{\tau}_p$ defined as

$$\boldsymbol{\tau}_{\mathrm{p}} = \boldsymbol{\mathcal{A}}\boldsymbol{k}_{\mathrm{LES}}. \tag{12}$$

3.2. Virtual Cloud Fields and Sky Images

The 3-D reconstruction methods are tested in the virtual testbed from Kurtz et al. (2017). This virtual testbed uses the University of California, Los Angeles (UCLA) LES (Stevens, 2010) to model a realistic 3-D atmospheric boundary layer with continental cumulus clouds at high resolution for a time period of 24 hours. Periodic boundary conditions represent infinite domains with the same ground cover, which allows the cloud and atmospheric turbulence to spin up and create realistic cloud shapes and dynamics such as condensation, evaporation and deformation. From the LES run, 3D liquid water content (LWC) of two representative time instances (at 4:38 h and 6:57 h after initialization) with cloud fractions of 6.8% and 33.3% are selected for reconstruction. Cloud fraction is defined as the fraction of grid points occupied by clouds in a vertical projection of the cloud field.

The LES LWC is input into the SHDOM (Evans, 1998) to produce radiance fields (I^{meas}) at a constant solar zenith angle (SZA) of 45°. The SHDOM radiance field reproduces a 1701 × 1701 pixel sky image as would be obtained through a fisheye lens with an equisolid angle projection (Miyamoto, 1964)

$$r' = 2f\, sin\left(\frac{\vartheta_p}{2}\right), \tag{13}$$

where f is the focal length, and r' is the distance from the principal point in the image plane. Three different wavelengths are simulated corresponding to the peak responses of the SI camera's red (620 nm), green (520 nm) and blue (450 nm) channels. The aerosol phase function, background Rayleigh and aerosol optical depths are obtained from the yearly average Aerosol Robotic Network (AERONET) measurements (Holben et al., 1998) as in Mejia et al. (2016). Spectral surface reflectances of 0.043, 0.068, and 0.071 were used for the blue, green and red channel simulations, respectively (Markham, 1992; Mejia et al., 2016). The cloud droplet effective radius, which is the area weighted mean radius of the cloud droplets, is 8 µm (Min, 2003) and defines the single scattering properties of the clouds in the SHDOM simulations. SHDOM simulations use open boundary conditions (Evans, 2015, 1998), which means that measurements outside the LES domain are not used for reconstruction.

3.3. Sky Imager Deployment Layouts

A sensitivity study elucidates the tradeoffs between different SI deployment variables, specifically the number and distance between imagers. A similar study by Huang et al., (2008) with MWR tomography found that the optimal number of MWR was 4, and that the optimal distance between MWR was 4 km. Nguyen and Kleissl (2014) demonstrated that the optimal distance between imagers for stereography is directly related to the CBH; therefore the optimal distance between imagers is expected to apply only for the CBH of our test case, which is 0.94 km.

To compare the tradeoffs of using multiple imagers, we simulated 2, 3, 4, 5 and 9 imagers arranged as outlined in Figure 5. To obtain the optimal distance between imagers, we tested setups of 2, 3, 4, 5 and 9 imagers evenly spaced from the center of the domain at distances $L = [0.25\ 0.5\ 1.0\ 1.5\ 2.0\ 3.0\ 4.0\ 6.0]$ km for the 2, 3, 4 and 5 imager setup, and $L = [0.25\ 0.5\ 1.0\ 1.5\ 2.0\ 3.0]$ km for the 9 imager setup. The dependence of reconstruction errors on the optimal number of imagers was analyzed with the respective spacings that minimized reconstruction error.

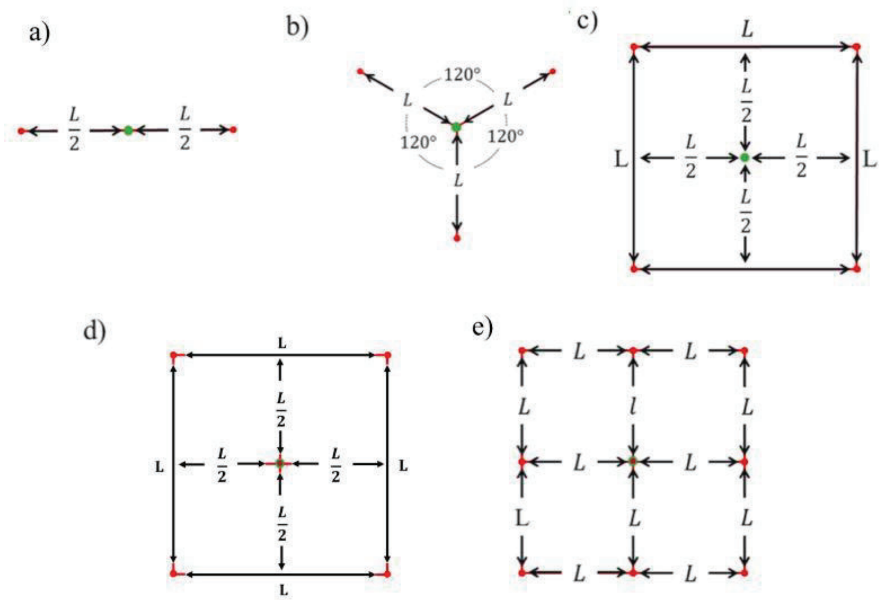

Figure 5. Layout of sky imager deployments with different number of imagers and distance (L) between imagers, a) 2 imagers along the x-axis, b) 3 imagers, c) 4 imagers, d) 5 imagers and e) 9 imagers. Red dots represent imager locations, and the green circle (green outline when imager located at center of domain) represents the center of domain.

3.4. Error Metrics

Since measuring cloud properties of real clouds is extremely challenging, the main benefit of using simulated test cases is the validation against spatially-resolved cloud properties. To this end, we are interested in analyzing errors in extinction coefficient, image red (620 nm) pixel brightness (PB) and surface Global Horizontal Irradiance (GHI). The red PB has been arbitrarily selected, however, any of the red, green, blue channels could be used. While perfect $\boldsymbol{k}$ retrievals would automatically result in perfect image PB and surface GHI, erroneous $\boldsymbol{k}$ retrievals may have different impacts on GHI and image errors, which are more relevant in the practice of solar forecasting. We will quantify these errors by calculating the domain mean absolute error (MAE) and mean bias error (MBE), defined as

$$\mathrm{MAE} = \frac{\overline{|\boldsymbol{k}_{\mathrm{LES}} - \boldsymbol{k}|}}{\overline{\boldsymbol{k}_{\mathrm{LES}}}}, \tag{14}$$

$$\mathrm{MBE} = \frac{\overline{\boldsymbol{k} - \boldsymbol{k}_{\mathrm{LES}}}}{\overline{\boldsymbol{k}_{\mathrm{LES}}}}, \tag{15}$$

where $\boldsymbol{k}$ can also be replaced with GHI or PB. For $\boldsymbol{k}$, the spatial averages (denoted by overbars) are over all LES grid points. For GHI, the averages are over surface grid points in x and y. For PB, the averages are over all pixels of all sky images.

4. Results

4.1 Nine Imager Validation

We validate the ART and iterative methods on the 9 imager deployment with a separation of 1.5 km against the ground truth $\boldsymbol{k}_{\mathrm{LES}}$ for the two cloud fraction cases. A perfect τ_{p} as defined in Eq. 12 is input to the ART. Figure 6 shows $\mathrm{MAE_k}$ as a function of the number of iterations. The initial $\boldsymbol{k}$ guess results in a large reconstruction error, but the ART method decreases the $\boldsymbol{k}$ MAE to 1.2% and 0.02% after 5 x 10^7 iterations for a 33% and 6.8% cloud fraction (CF), respectively. The error for the high CF case continues to decrease after 5 x 10^7 iterations while the low CF case converges to zero $\mathrm{MAE_k}$ after only 1 x 10^7 iterations. Any additional cloud will block the view of other clouds in several imagers and limit the observability of cloud tops and clear sky voxels in the domain, requiring disproportionally more iterations to arrive at the solution. In the extreme case of an overcast cloud layer, cloud top heights could not be reconstructed at all.

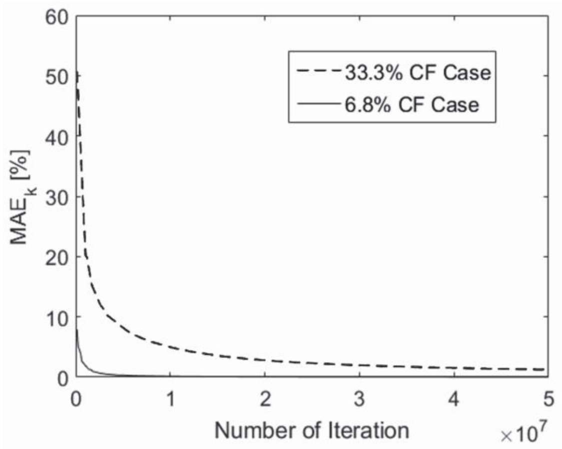

Figure 6. Convergence of ART as indicated by the mean absolute error of the extinction coefficients. 33.3% and 6.8% CF test cases are the dashed and solid lines, respectively.

Figure 7 validates the iterative reconstruction method. We input $\boldsymbol{k}$ output from the ART method. To validate the correct implementation of the iterative method, we eliminate the largest source of error by assuming that the source function J of the ground truth cloud field is known. Therefore referring to Figure 3 the gradient descent iteration loop is not required and only the constant source function iteration is executed. Figure 7 demonstrates that the iterative method converges to 0.2% $\boldsymbol{k}$ MAE after 2 x 10^7 iterations, significantly below the 1.2% $\boldsymbol{k}$ MAE of the ART alone (Figure 6). The image MAE converges faster, but remains slightly larger at 0.3%. However, each iteration with the iterative method takes significantly longer than an iteration with the ART method (see next section).

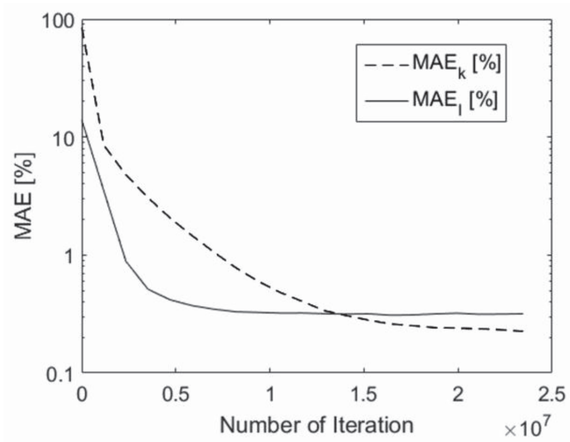

Figure 7. Convergence of iterative method $\boldsymbol{k}$ (dashed) and image (solid) mean absolute errors for the 33% CF case.

4.2. Optimal Deployment

4.2.1. Optimal Sky Imager Distance

The ART method is used to analyze optimal deployments because of its low computation cost. Using an Intel Core i7-3770 3.4GHz computer, 9 imagers, and a cloud fraction of 2.3%, the ART method yields converged results within about 30 seconds as opposed to 6 days with the iterative method, which corresponds to a factor of 2×10^4 difference in speed. The ART method (Section 3.1) is applied on a perfect τ_p as defined in Eq. 12. Figure 8 shows that the accuracy of the retrieved $\boldsymbol{k}$ increases with the distance between imagers. GHI and image pixel brightness MAE, on the other hand, do not improve for spacings larger than 1.5 km. The error decreases the most between $L = 0.25$ km and $L = 0.5$ km. The Appendix demonstrates the distance results for 4 and 2 imagers, respectively (Figure A1 and Figure A2). The results for 4 imagers are consistent with Huang et al., (2008) with an optimum between 2 km $< L <$ 4 km for $\boldsymbol{k}$. GHI and image error perform worse as L increases beyond 4 km. The 2-imager setup continues to improve with increased separation.

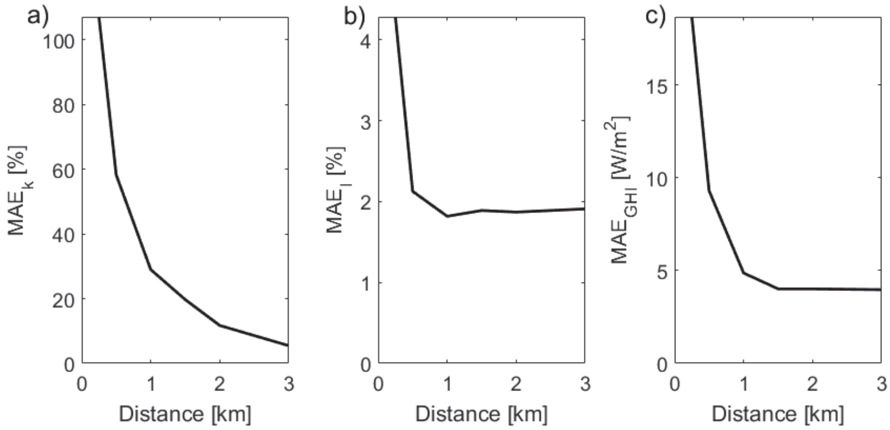

Figure 8. Domain averaged mean absolute error in (a) $\boldsymbol{k}$, (b) image pixel brightness, and (c) Global Horizontal Irradiance (GHI) for retrievals with 9 imagers at different distances L.

4.1.2. Optimal Number of Sky Imagers

Figure 9 shows that increasing the number of SIs improves the overall reconstruction of the cloud domain. Similar to Huang et al. (2008), we observe a large performance increase when using 4 imagers compared to 2 or 3, and less improvement with additional imagers.

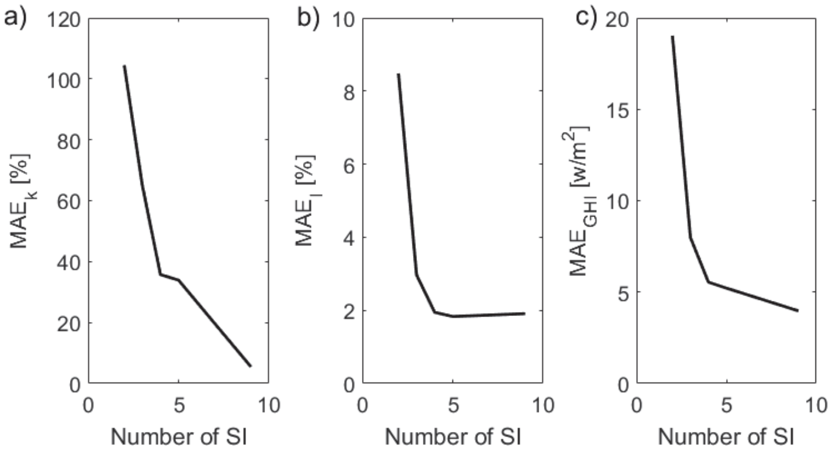

Figure 9. Domain averaged mean absolute error in (a) extinction coefficient ***k***, (b) image pixel brightness, and (c) Global Horizontal Irradiance (GHI) for retrievals with 2, 3, 4, 5 and 9 imagers at their respective optimal separations.

Although improvements in GHI and image pixel error between 4 and 9 imagers are minimal for an ideal case, using 9 imagers improves the robustness of the cloud scene reconstruction in real applications. Two mechanisms are expected to benefit tomographic methods applied to 4 or more imagers in real applications. The first benefit is that dirt on the dome of one imager does not contaminate the results. In single-imager cloud decision, dirt is often identified as a cloud since its red-blue-ratio is closer to clouds than the clear sky. Reconstruction limits the impact of dirt because the only solution that can satisfy a "cloud" in one image that is not present in any other images is a "cloud" located immediately above the imager. Such a low 'cloud' would be invisible to the other imagers as data at large pixel zenith angles is poorly resolved and therefore excluded. Thus, the constraint on minimum CBH results in the clearing of that cloud (see Section 2.4).

The second benefit is that using data from the circumsolar region becomes unnecessary. As stated in Section 2.1, the circumsolar region in the sky hemisphere is a common source of cloud identification error. With 9 imagers, it is possible to ignore the circumsolar region in every imager as the neighboring imagers are able to fill in the missing data for the circumsolar region. Figure 9a and Figure **10** demonstrate that in an ideal case (no circumsolar region errors), the ***k*** MAE only decreases to 5% from 35%. Removing the pixels with less than a 30 degree solar pixel angle (also referred to as scattering angle) in each image (Figure 10), the ***k*** MAE decreases to 15% from 80%, i.e. a much larger improvement in percentage points for 9 imagers compared to 5 or less imagers. This result suggests that for real deployments at least 9 imagers are recommended.

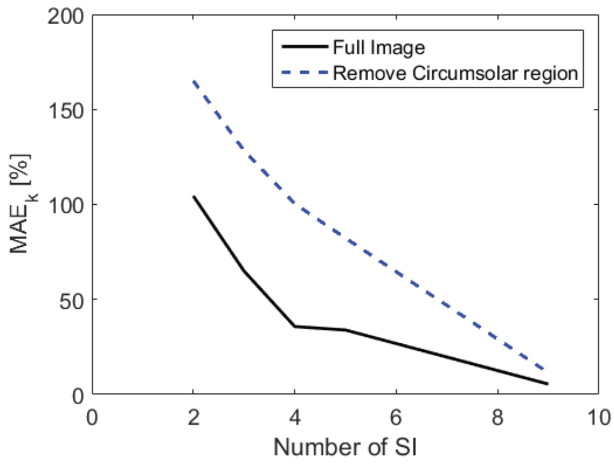

Figure 10. Domain averaged $\boldsymbol{k}$ MAE for retrievals with 2, 3, 4 and 9 imagers using the full image (same as Figure 9a) in black and removing the circumsolar region with solar pixel angle $\boldsymbol{\vartheta}_s < 30°$ in each image in dashed blue.

4.2. 3D Reconstruction Methods

To isolate characteristics of the reconstruction methods, we now focus on a specific deployment with 9 imagers spaced at L = 1.5 km. We use 9 imagers because this is the optimum scenario to demonstrate the limitations of the methods and not the deployments, while maintaining $L = 1.5$ km (versus $L = 3$ km) since it becomes increasingly difficult to obtain permissions to install camera systems away from the location of interest. For example, at a utility scale power plant with a typical dimension of 2 × 2 km, $L =$ 3 km would require obtaining permissions from up to 5 adjacent property owners.

4.2.1. Algebraic Reconstruction Technique

As described in Section 2.2, the ART method requires an input $\boldsymbol{\tau}$ to calculate $\boldsymbol{k}$. Unlike in Section 4.1 where the τ_{p} input was assumed to be error-free based on Eq. 12, here the RRBR method provides the initial $\boldsymbol{\tau}$ (Mejia et al., 2016). The RRBR method uses both radiance and red blue ratio values to estimate $\boldsymbol{\tau}$ based on a look-up table of SHDOM simulations of homogenous clouds. Since the RRBR is based on homogeneous clouds, it has a propensity to underestimate $\boldsymbol{\tau}$ because homogeneous clouds are darker than heterogeneous clouds on average. This underestimation in $\boldsymbol{\tau}$ is seen in Figure 11 and Table 1 as the $\boldsymbol{k}$ MBE is -17.1%. Figure 11 shows that the spatial distribution and size of clouds by the ART method correspond broadly with the ground truth, but small differences in location and size cause a MAE for $\boldsymbol{k}$ is 53.4% while the GHI MAE is significantly smaller at 1.53%.

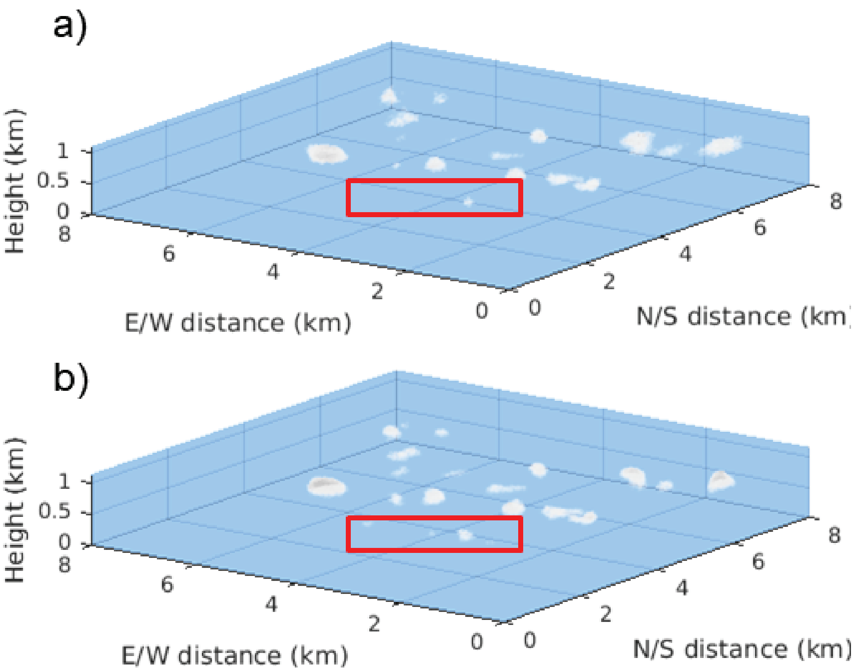

Figure 11. 3-D depiction of reconstructed $\boldsymbol{k}$ from (a) the Algebraic Reconstruction Technique (ART) (a) and ground truth (b). The red boxes highlight an area where the extinction coefficients are underestimated by the ART method.

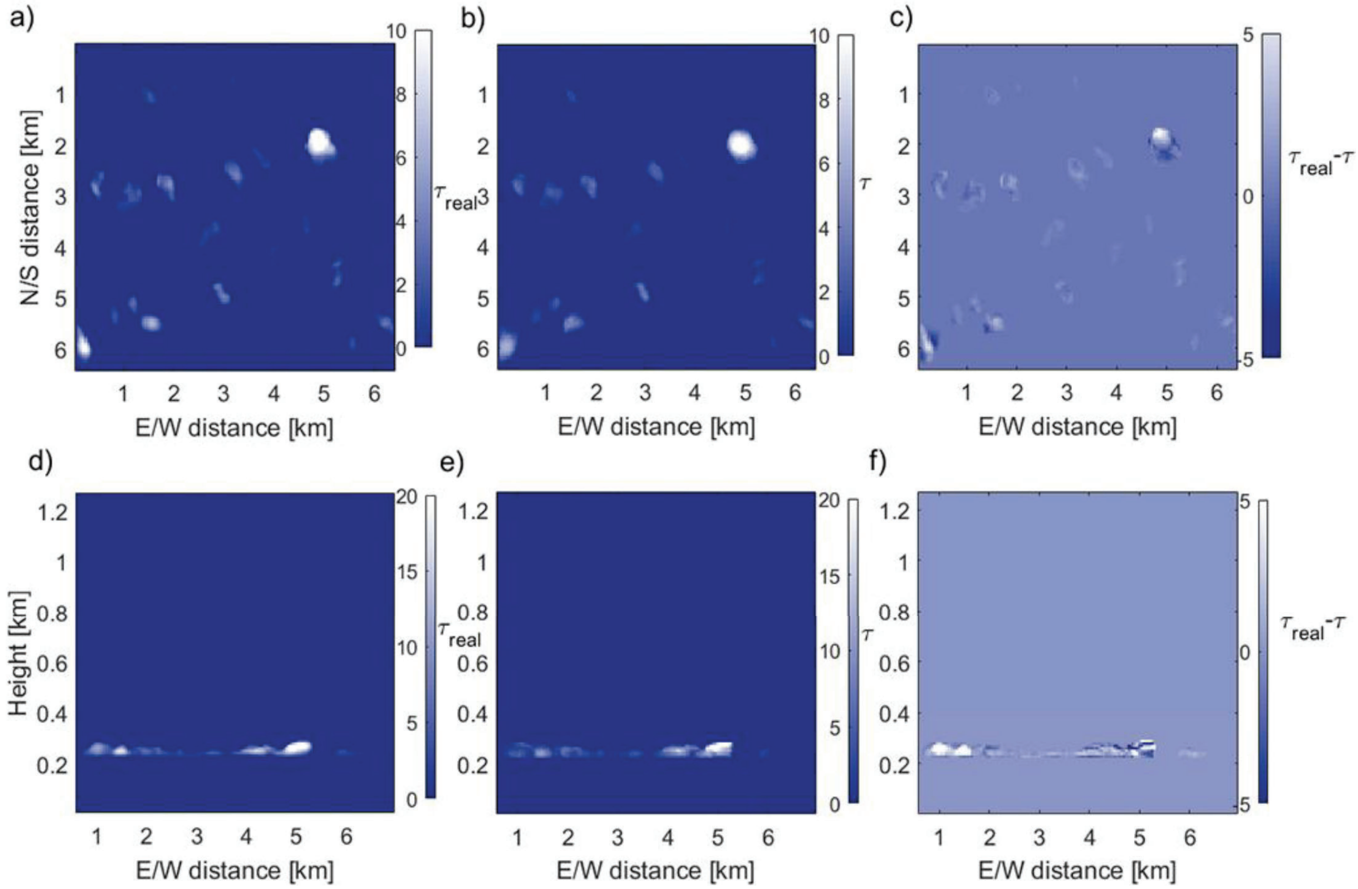

Figure 12. Vertical sum (a, b, and c) and North-South sum (d, e, and f) of $\boldsymbol{k}$ (equivalent to $\boldsymbol{\tau}$) for CF of 6.8% from LES (ground truth; a and d); reconstructed from Algebraic Reconstruction Technique (ART; b and e); and their difference (c and f). North (N) is up and East (E) is to the right per convention.

Table 1. Error statistics of Algebraic Reconstruction Technique (ART) and iterative method for a CF of 6.8%. rMAE [%] is the relative mean absolute error, and rMBE [%] is the relative mean bias error. DNI is the Direct Normal Irradiance and GHI is the Global Horizontal Irradiance. $\boldsymbol{k}$ is the extinction coefficient and $\boldsymbol{\tau}$ is the vertical sum of $\boldsymbol{k}$.

	ART			**Iterative method**		
	rMAE [%]	MAE	rMBE [%]	rMAE [%]	MAE	rMBE [%]
$\boldsymbol{\tau}$	34.80	0.0481 [-]	17.10	17.20	0.0238 [-]	2.80
$\boldsymbol{k}$	53.40	0.00025 [-]	17.10	33.60	0.00015 [-]	2.80
GHI	1.53	10.10 W m^{-2}	0.04	0.85	5.6 W m^{-2}	-0.12
GHI ($GHI / GHI_{clear} < 0.98$)	21.80	68.90 W m^{-2}	-14.20	0.86	2.70 W m^{-2}	-0.15
DNI	1.30	10.50 W m^{-2}	-0.46	0.81	6.50 W m^{-2}	-0.21
Image pixel red channel	4.30	-	1.30	0.70	-	0.60

Removing all (cloud-free) grid points with $GHI / GHI_{clear} > 0.98$, the rMAE of GHI increases to 21.8%. Most cloudy grid points are correctly identified with 98.8% of $\boldsymbol{k}$, being correctly separated as $\boldsymbol{k} = 0$ or

$\boldsymbol{k} \neq 0$ (Table 2). $\boldsymbol{k}$ voxels that are misidentified are either thin clouds ($\tau < 0.5$), e.g. in the north west of the domain (as seen in Figure 11 inside the red box) or at the edges of clouds.

Table 2. Contingency table of observed extinction coefficient and reconstructed Algebraic Reconstruction Technique (ART) extinction coefficient, $\boldsymbol{k}$ for CF = 6.8%.

		Observation	
		$\boldsymbol{k} = 0$	$\boldsymbol{k} \neq 0$
ART	$\boldsymbol{k} = 0$	94%	0.8%
	$\boldsymbol{k} \neq 0$	0.4%	4.8%

4.2.2. Iterative Retrieval

The iterative method is based on the assumption that iteratively minimizing the image error further minimizes the extinction coefficient errors. To decrease the computational cost, $\boldsymbol{k}$ from the ART method is input to the iterative method providing an accurate first estimate. Unlike in Section 4.1 the source function is not assumed to be known. Therefore the full bi-level iteration presented in Figure 3 is executed. Figure 13 and Table 1 demonstrate that the iterative method further decreases the image error. After 13 iterations, the image rMAE decreases from 4.3% to 0.7% and 13.2% to 7.0% for the 6.8% and 33.3% CF cases, respectively. The $\boldsymbol{k}$ rMAE also decreases from 53.4% to 33.6% and 83.2% to 66.4% for the 6.8% and 33.3% CF cases, respectively.

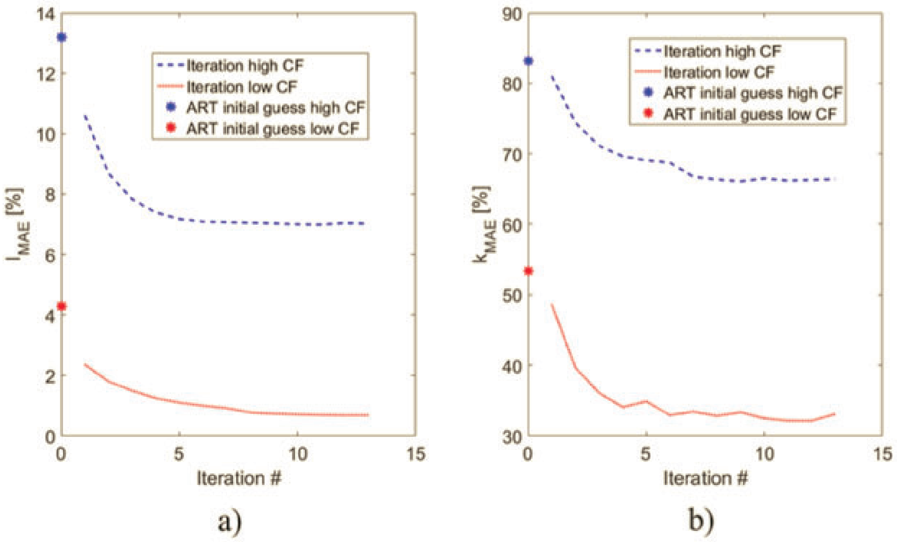

Figure 13. Mean average error for each iteration for the iterative method. a) Image pixel brightness; b) extinction coefficient.

The iterative method decreases the error from the initial ART estimate. For the small CF case $\boldsymbol{k}$ rMAE decreases nearly 20 percentage points, or 36%. The over-predictive tendencies are resolved with the $\boldsymbol{k}$ rMBE improving from 17.1% to 2.8%, the GHI rMAE of cloudy regions improving from 21.8% to 0.85%, and the GHI rMBE of cloudy regions improving from 14.2% to 0.15%.

4.3. Solar Forecasting

Table 1 demonstrates that the rMAE in GHI is minor compared to the error in $\boldsymbol{k}$ for both the ART and the iterative method. For atmospheric science applications, the $\boldsymbol{k}$ error magnitude indicates that the current methods require further improvements to provide high quality 3-D cloud reconstructions. For solar energy applications, since surface GHI is the relevant quantity the ART method appears to be sufficient.

To demonstrate the potential of the ART for solar forecasting applications, the GHI map from the ART method in section 4.2 is advected using the average cloud speed from the LES. Figure 14 demonstrates rMAE of persistence, conventional single SI, and the ART forecasts relative to the ground truth measurements from the LES. The conventional SI forecast consists of a 2-D cloud representation and trinary (clear, thin cloud, thick cloud) cloud decision (Yang et al., 2014). The ART method significantly improves upon the conventional method throughout the 5 minutes forecast horizon. The improvements are due to better representation of 3-D clouds as well as the more accurate representation of cloud optical depth compared to the trinary system. At longer forecast times, the clouds evolve in shape and thickness, and the advantage of better initial cloud conditions decreases. The accuracy of persistence forecasts decreases for that same reason and for forecast horizons of 1 to 5 min, the ART rMAE then beats persistence.

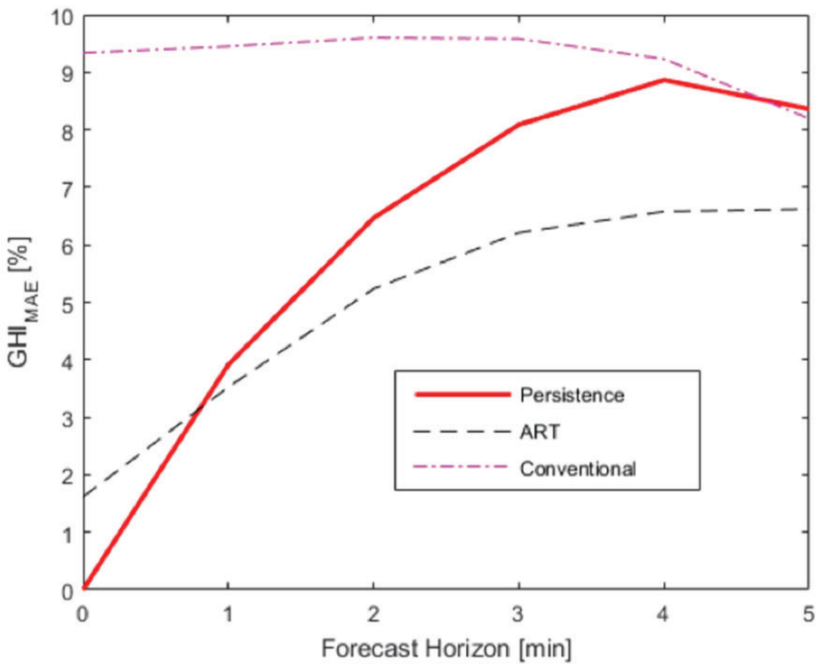

Figure 14. Global Horizontal Irradiance (GHI) forecast mean average error (MAE) for persistence forecast in red, conventional forecast (Yang et al., 2014) in magenta (dot-dashed), and Algebraic Reconstruction Technique (ART) forecast in black (dashed). The persistence forecast assumes that the current GHI persists for the next 5 minutes.

5. Discussion and Conclusions

This paper introduces the application of tomographic methods to multiple sky images to reconstruct 3-D fields of extinction coefficients. Virtual images are created by simulating 3-D heterogeneous cloud scenes in the atmospheric boundary layer using LES. As expected, more imagers increase the accuracy of 3-D cloud reconstruction, especially for up to 4 imagers after which the benefits of additional imagers decrease. However, more imagers increase robustness to imager soiling and cloud detection errors in the circumsolar region of images. Although having more imagers improves the accuracy of the 3-D reconstruction, it also increases the capital, operations, and maintenance cost of the imagers, creating a tradeoff between more imagers and improved accuracy. The distance between imagers also plays an important role in reconstruction accuracy. In idealized scenarios with a 0.94 km cloud base height, an increase in separation between imagers led to an increase in 3-D reconstruction accuracy up to 3 km. This is because a diversity in view perspectives better constrains cloud dimensions.

Summary statistics of the ART and the iterative methods are presented in Table 1. The $\boldsymbol{k}$ rMAE is 53.4% using the ART and decreases to 33.6% after 13 iterations of the iterative method. The ART method, using $\boldsymbol{\tau}$ from the RRBR method, inherits the cloud optical depth under-predicting tendency of the RRBR as demonstrated by the -17.1% rMBE of $\boldsymbol{k}$. Although the iterative method decreases the rMBE, the computational cost of several days to reconstruct a single cloud scene renders the method unusable for solar forecast applications. Computational costs increase with higher cloud fraction as more cloud voxels must be solved. On the other hand, the ART method takes only about 30 seconds, which is compatible with solar forecast application. The ART method beats persistence forecast already at a 1-minute forecast horizon, demonstrating its potential for solar energy applications.

It is important to note that these conclusions are for an idealized image and the results need to be validated in real images as well to account for both topographic obstructions and non-ideal lens distortion. Since buildings and trees commonly obstruct the horizon in an image, imagers where the cloud appears at a large zenith angle (near the horizon) may not contribute to the reconstruction of that cloud. Furthermore, cases with clouds obstructed by other clouds as in multiple cloud layers need to be investigated. Further, the sensitivity of the reconstruction accuracy to the surface albedo should be established given the abundant installation of utility-scale solar power plants near more reflective arid and semi-arid surfaces.

Acknowledgements

We acknowledge funding from the California Energy Commission EPIC program. Felipe Mejia was supported by the National Science Foundation Graduate Research Fellowship under Grant No. (DGE-1144086).

References

Aides, A., Schechner, Y.Y., Holodovsky, V., Garay, M.J., Davis, A.B., 2013. Multi sky-view 3D aerosol distribution recovery. Opt. Express 21, 25820. doi:10.1364/OE.21.025820

Chow, C.W., Belongie, S., Kleissl, J., 2015. Cloud motion and stability estimation for intra-hour solar forecasting. Sol. Energy 115, 645–655. doi:10.1016/j.solener.2015.03.030

Evans, F., 2015. Spherical Harmonic Discrete Ordinate Method (SHDOM) radiative transfer model [WWW Document]. Accessed 2018-06-08. URL http://nit.colorado.edu/shdom/shdomdoc/ (accessed 6.8.18).

Evans, K.F., 1998. The Spherical Harmonics Discrete Ordinate Method for Three-Dimensional Atmospheric Radiative Transfer. J. Atmos. Sci. 55, 429–446. doi:10.1175/1520-

0469(1998)055<0429:TSHDOM>2.0.CO;2

Gordon, R., Bender, R., Herman, G.T., 1970. Algebraic reconstruction techniques (ART) for three-dimensional electron microscopy and x-ray photography. J. Theor. Biol. 29, 471–481. doi:10.1016/0022-5193(70)90109-8

Hammer, A., Heinemann, D., Westerhellweg, A., 1999. Daylight and solar irradiance data derived from satellite observations - The satellight project, in: Proc. EUMETSAT Meteorological Satellite Data Users Conference. pp. 331–337.

Holben, B.N., Eck, T.F., Slutsker, I., Tanré, D., Buis, J.P., Setzer, A., Vermote, E., Reagan, J.A., Kaufman, Y.J., Nakajima, T., Lavenu, F., Jankowiak, I., Smirnov, A., 1998. AERONET—A Federated Instrument Network and Data Archive for Aerosol Characterization. Remote Sens. Environ. 66, 1–16. doi:10.1016/S0034-4257(98)00031-5

Holodovsky, V., Schechner, Y.Y., Levin, A., Levis, A., Aides, A., 2016. In-situ multi-view multi-scattering stochastic tomography. 2016 IEEE Int. Conf. Comput. Photogr. ICCP 2016 - Proc. doi:10.1109/ICCPHOT.2016.7492869

Huang, D., Liu, Y., Wiscombe, W., 2008. Determination of cloud liquid water distribution using 3D cloud tomography. J. Geophys. Res. Atmos. 113, 1–13. doi:10.1029/2007JD009133

Kurtz, B.B., 2017. Solar Resource Assessment with Sky Imagery and a Virtual Testbed for Sky Imager Solar Forecasting. University of California San Diego.

Levis, A., Schechner, Y.Y., Aides, A., Davis, A.B., 2015. Airborne three-dimensional cloud tomography. Proc. IEEE Int. Conf. Comput. Vis. 2015 Inter, 3379–3387. doi:10.1109/ICCV.2015.386

Levis, A., Schechner, Y.Y., Davis, A.B., 2017. Multiple-Scattering Microphysics Tomography, in: The IEEE Conference on Computer Vision and Pattern Recognition (CVPR). pp. 6740–6749.

Lorenz, E., Remund, J., Müller, S.C., Traunmüller, W., Steinmaurer, G., Pozo, D., Ruiz-Arias, J.A., Fanego, V.L., Ramirez, L., Romeo, M.G., Kurz, C., Pomares, L.M., Guerrero, C.G., 2009. Benchmarking of Different Approaches to Forecast Solar Irradiance, in: 24th European Photovoltaic Solar Energy Conference. pp. 4199–4208.

Markham, B.L., 1992. Surface Reflectance Retrieval From Satellite and Aircraft Results of Sensor and Algorithm Comparisons During FIFE. J. Geophys. Res. 97, 18,785-18,795.

Martín, A., Trapero, J.R., 2015. Recursive Estimation Methods to Forecast Short-Term Solar Irradiation, in: Lefebvre G., Jiménez E., Cabañas B. (Eds) Environment, Energy and Climate Change II. The Handbook of Environmental Chemistry, Vol 34. Springer, Cham. pp. 41–53. doi:10.1007/698

Mathiesen, P., Collier, C., Kleissl, J., 2013. A high-resolution, cloud-assimilating numerical weather prediction model for solar irradiance forecasting 92, 47–61. doi:10.1016/j.solener.2013.02.018

Mathiesen, P., Kleissl, J., 2011. Evaluation of numerical weather prediction for intra-day solar forecasting in the continental United States. Sol. Energy 85, 967–977. doi:10.1016/j.solener.2011.02.013

Mejia, F.A., Kurtz, B., Murray, K., Hinkelman, L.M., Sengupta, M., Xie, Y., Kleissl, J., 2016. Coupling sky images with radiative transfer models: A new method to estimate cloud optical depth. Atmos. Meas. Tech. 9, 4151–4165. doi:10.5194/amt-9-4151-2016

Min, Q.-L., 2003. Validation of surface retrieved cloud optical properties with in situ measurements at the

Atmospheric Radiation Measurement Program (ARM) South Great Plains site. J. Geophys. Res. 108, 4547. doi:10.1029/2003JD003385

Miyamoto, K., 1964. Fish Eye Lens. J. Opt. Soc. Am. 54, 1060. doi:10.1364/JOSA.54.001060

Nguyen, D., Kleissl, J., 2014. Stereographic methods for cloud base height determination using two sky imagers. Sol. Energy 107, 495–509. doi:10.1016/j.solener.2014.05.005

Oberländer, J., Pfotzer, L., Roennau, A., Dillmann, R., 2015. Fast calibration of rotating and swivelling 3-D laser scanners exploiting measurement redundancies. IEEE Int. Conf. Intell. Robot. Syst. doi:10.1109/IROS.2015.7353796

Peng, Z., Yu, D., Huang, D., Heiser, J., Yoo, S., Kalb, P., 2015. 3D cloud detection and tracking system for solar forecast using multiple sky imagers. Sol. Energy 118, 496–519. doi:10.1016/j.solener.2015.05.037

Quesada-Ruiz, S., Chu, Y., Tovar-Pescador, J., Pedro, H.T.C., Coimbra, C.F.M., 2014. Cloud-tracking methodology for intra-hour DNI forecasting. Sol. Energy 102, 267–275. doi:10.1016/j.solener.2014.01.030

Schmidt, T., Kalisch, J., Lorenz, E., Heinemann, D., 2015. Evaluating the spatio-temporal performance of sky imager based solar irradiance analysis and forecasts. Atmos. Chem. Phys. Discuss. 15, 26997–27039. doi:10.5194/acpd-15-26997-2015

Seeram, E., 2015. Chapter 3: Physical Principles of CT, in: Computed Tomography 4th Edition Physical Principles, Clinical Applications, and Quality Control. p. 576.

Stevens, B., 2010. Introduction to UCLA-LES [WWW Document]. Accessed 2018-06-08. doi:10.1007/978-1-4419-6169-3

Sun, X.J., Li, H.R., Barker, H.W., Zhang, R.W., Zhou, Y.B., Liu, L., 2016. Satellite-based estimation of cloud-base heights using constrained spectral radiance matching. Q. J. R. Meteorol. Soc. 142, 224–232. doi:10.1002/qj.2647

Urquhart, B., Ghonima, M., Nguyen, D.A., Kurtz, B., 2013. Sky-Imaging Systems for Short-Term Forecasting, in: Solar Energy Forecasting and Resource Assessment. pp. 195–232. doi:10.1016/B978-0-12-397177-7.00009-7

Urquhart, B., Kurtz, B., Dahlin, E., Ghonima, M., Shields, J.E., Kleissl, J., 2015. Development of a sky imaging system for short-term solar power forecasting. Atmos. Meas. Tech. 8, 875–890. doi:10.5194/amt-8-875-2015

Urquhart, B., Kurtz, B., Kleissl, J., 2016. Sky camera geometric calibration using solar observations. Atmos. Meas. Tech. 9, 4279–4294. doi:10.5194/amt-9-4279-2016

Veikherman, D., Aides, A., Schechner, Y.Y., Levis, A., 2015. Clouds in the cloud. Lect. Notes Comput. Sci. (including Subser. Lect. Notes Artif. Intell. Lect. Notes Bioinformatics) 9006, 659–674. doi:10.1007/978-3-319-16817-3_43

Wang, G., Kurtz, B., Kleissl, J., 2016. Cloud base height from sky imager and cloud speed sensor. Sol. Energy 131, 208–221. doi:10.1016/j.solener.2016.02.027

Wu, X., Jin, S., Li, Y., Dong, Y., 2017. Voxel Nodes Model Parameterization for GPS Water Vapor Tomography, in: Sun J., Liu J., Yang Y., Fan S., Yu W. (Eds) China Satellite Navigation

Conference (CSNC) 2017 Proceedings: Volume I. CSNC 2017. Lecture Notes in Electrical Engineering, Vol 437. Springer, Singapore. pp. 3–12. doi:10.1007/978-981-10-4588-2

Yang, H., Kurtz, B., Nguyen, D., Urquhart, B., Chow, C.W., Ghonima, M., Kleissl, J., 2014. Solar irradiance forecasting using a ground-based sky imager developed at UC San Diego 103, 502–524.

Ye, S., Xia, P., Cai, C., 2016. Optimization of GPS water vapor tomography technique with radiosonde and COSMIC historical data. Ann. Geophys. 34, 789–799. doi:10.5194/angeo-34-789-2016

Zhong, X., Sahu, D.K., Kleissl, J., 2017. WRF inversion base height ensembles for simulating marine boundary layer stratocumulus. Sol. Energy 146, 50–64. doi:10.1016/j.solener.2017.02.021

Appendix

Figure A1 and Figure A2 are the equivalent of Figure 8 and demonstrate the improvements with increased separation for 4 and 2 imager deployments respectively. The results are consistent with Huang et al., (2008) with an optimum between 2 km < L < 4 km for $\boldsymbol{k}$. GHI and image error perform worse as L increases beyond 4 km. The 2-imager setup continues to improve with increased separation.

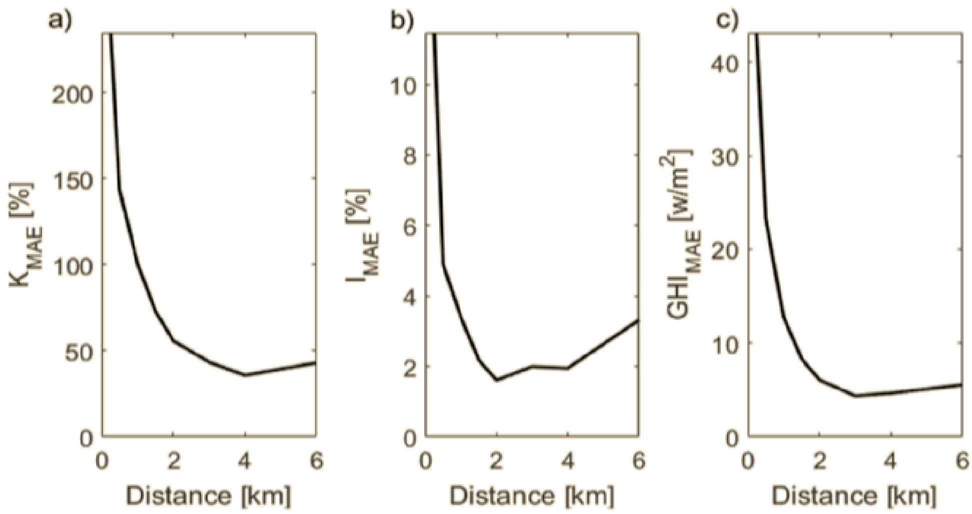

Figure A1. Domain averaged mean error in (a) $\boldsymbol{k}$, (b) image pixel brightness, and (c) Global Horizontal Irradiance (GHI) for retrievals with 4 imagers at different distances L.

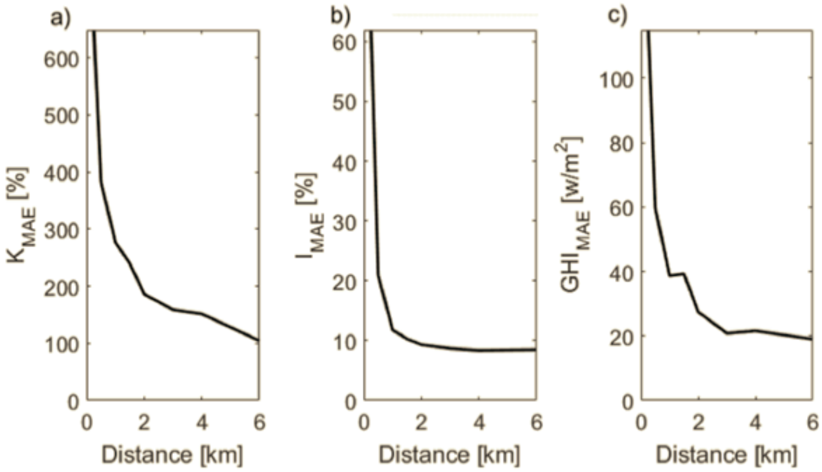

Figure A2. Domain averaged mean error in (a) $\boldsymbol{k}$, (b) image pixel brightness, and (c) Global Horizontal Irradiance (GHI) for retrievals with 2 imagers at different distances L.

Figure A3 through Figure A5 show the reconstructed spatial fields of clear sky index and two perspectives of the extinction coefficient $\boldsymbol{k}$. The results in Figure 8 are based on the data shown in these figures.

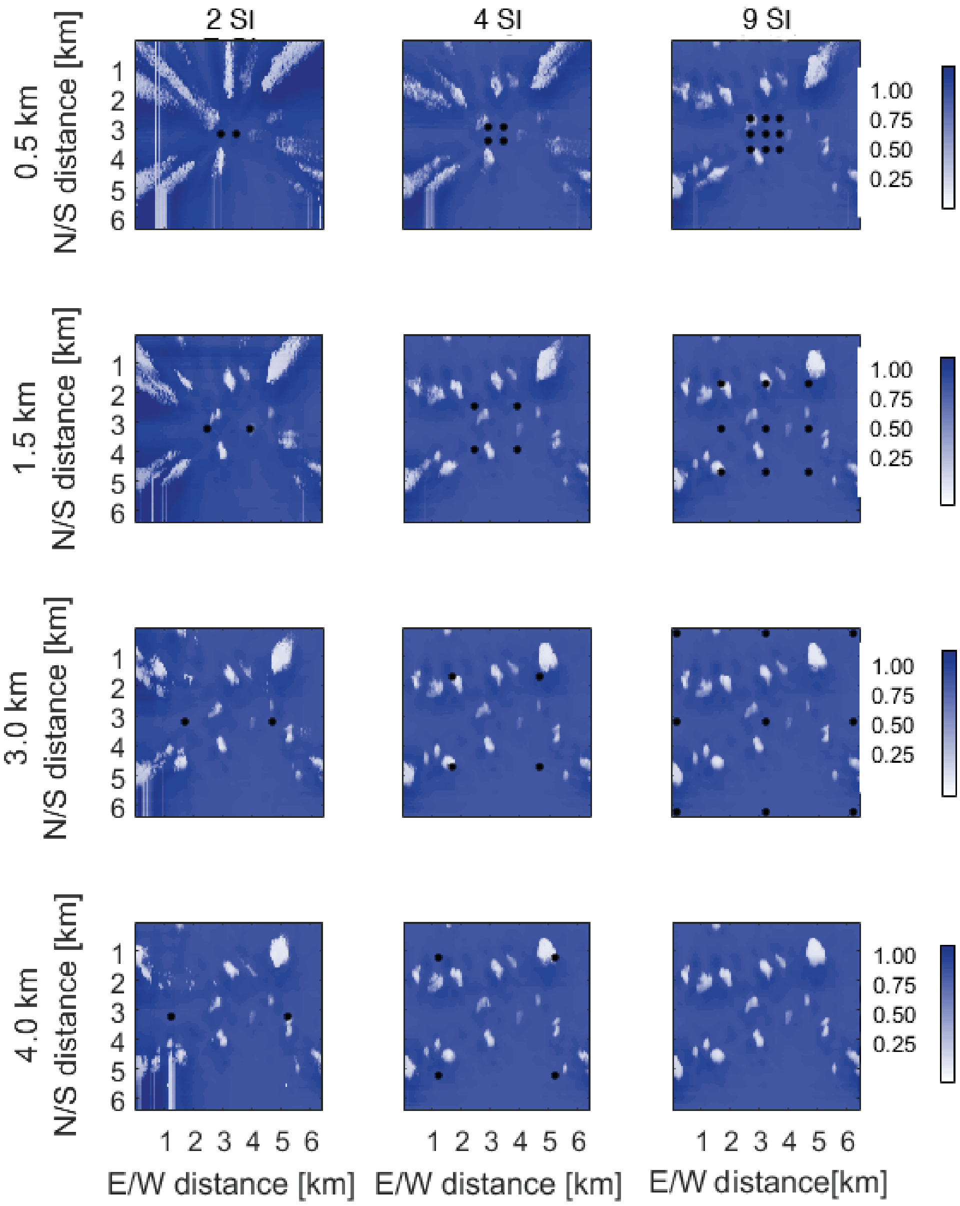

Figure A3. Spherical Harmonic Discrete Ordinate Method (SHDOM) simulated clear sky index at the surface from the reconstructed extinction coefficient field from different numbers of imagers (columns) at different spacing *L* (rows) for a CF of 6.8% using the ART method**.** Black dots represent imager locations. The bottom right image is ground truth from Large Eddy Simulation (LES).

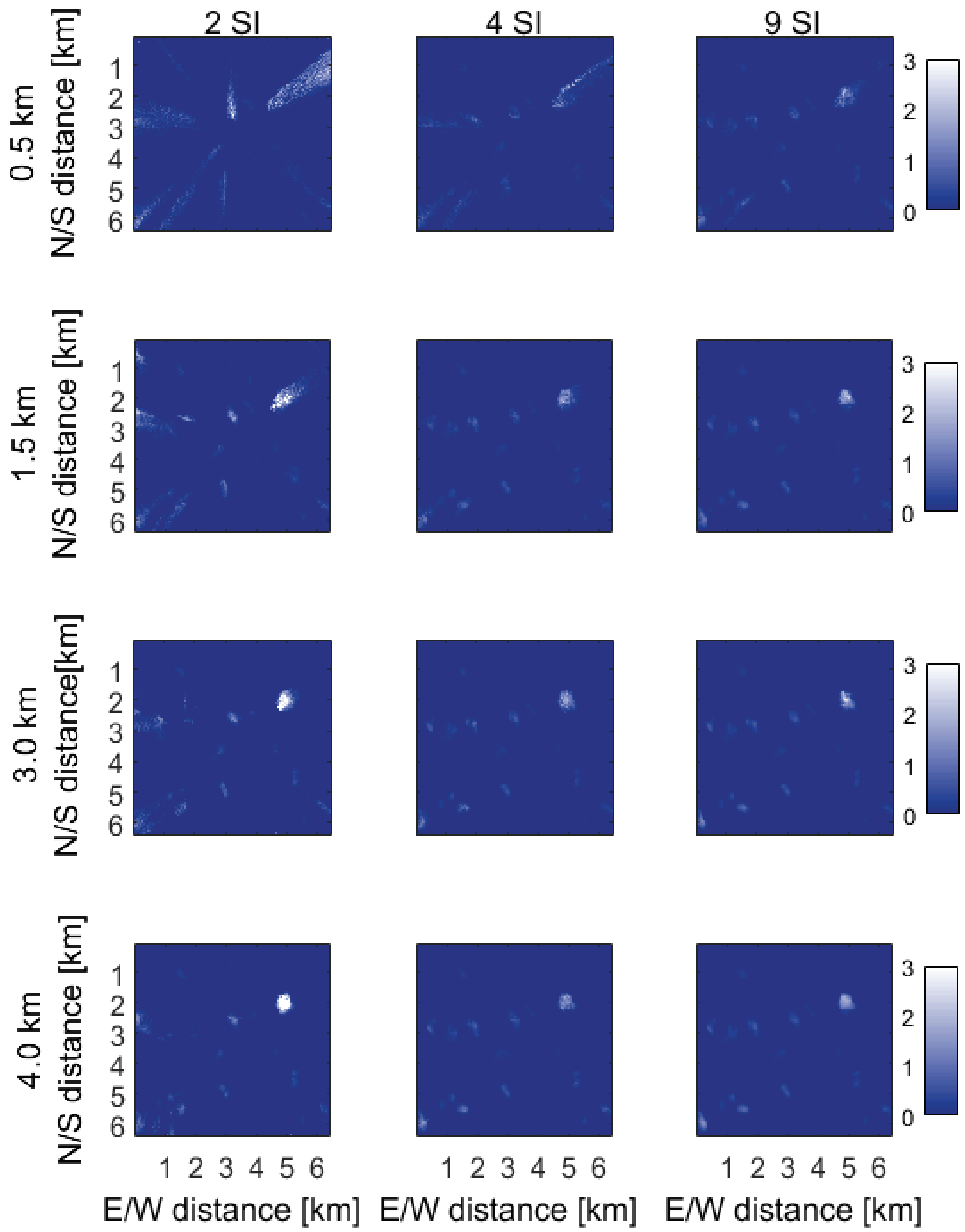

Figure A4. Reconstructed vertically averaged extinction coefficient ***k*** from different number of imagers (columns) at different spacings ***L*** (rows) for a CF of 6.8% using the ART method**.** The bottom right graph is the correct ***k***.

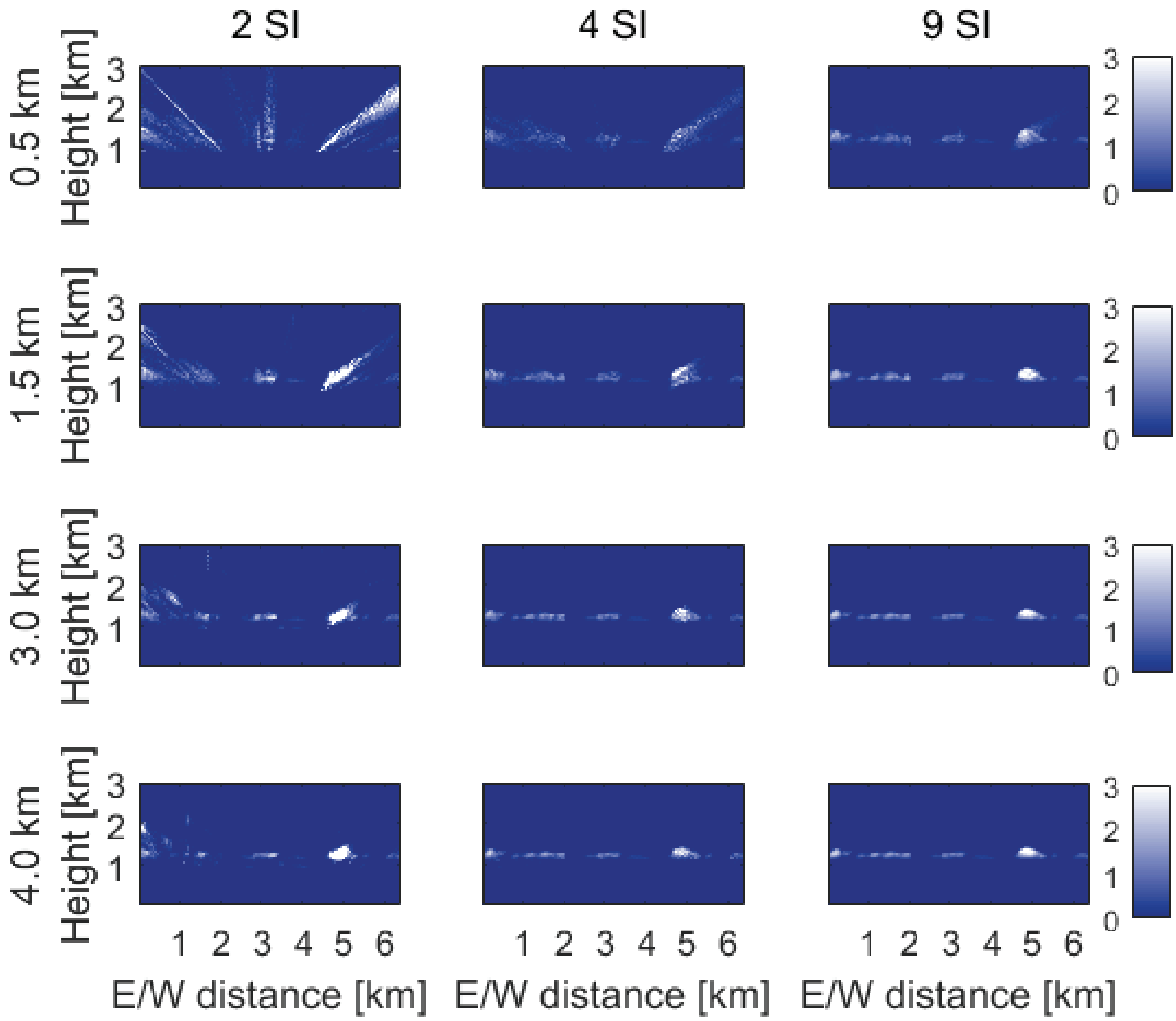

Figure A5. Reconstructed extinction $\boldsymbol{k}$ averaged in the North-South direction from different numbers of imagers (columns) at different spacings $\boldsymbol{L}$ (rows) for a CF of 6.8% using the ART method. The bottom right graph is the correct $\boldsymbol{k}$. The data shown is identical to Figure A4, but as a vertical slice rather than a top-down view.